Editors' Suggestion | Featured in Physics

Single-Crystal Alkali Antimonide Photocathodes: High Efficiency in the Ultrathin Limit

C. T. Parzyck,[1,*] A. Galdi,[2,*] J. K. Nangoi,[1] W. J. I. DeBenedetti,[3] J. Balajka,[3] B. D. Faeth,[4] H. Paik,[4] C. Hu,[1] T. A. Arias,[1] M. A. Hines,[3] D. G. Schlom,[5,6,7] K. M. Shen,[1,6] and J. M. Maxson[2,†]

[1]*Department of Physics, Laboratory of Atomic and Solid State Physics, Cornell University, Ithaca, New York 14853, USA*
[2]*Cornell Laboratory for Accelerator-Based Sciences and Education, Cornell University, Ithaca, New York 14853, USA*
[3]*Department of Chemistry and Chemical Biology, Cornell University, Ithaca, New York 14853, USA*
[4]*Platform for the Accelerated Realization, Analysis, and Discovery of Interface Materials (PARADIM), Cornell University, Ithaca, New York 14853, USA*
[5]*Department of Materials Science and Engineering, Cornell University, Ithaca, New York 14853, USA*
[6]*Kavli Institute at Cornell for Nanoscale Science, Cornell University, Ithaca, New York 14853, USA*
[7]*Leibniz-Institut für Kristallzüchtung, Max-Born-Straße 2, 12489 Berlin, Germany*

(Received 30 December 2021; accepted 2 February 2022; published 18 March 2022)

The properties of photoemission electron sources determine the ultimate performance of a wide class of electron accelerators and photon detectors. To date, all high-efficiency visible-light photocathode materials are either polycrystalline or exhibit intrinsic surface disorder, both of which limit emitted electron beam brightness. In this Letter, we demonstrate the synthesis of epitaxial thin films of Cs_3Sb on 3C-SiC (001) using molecular-beam epitaxy. Films as thin as 4 nm have quantum efficiencies exceeding 2% at 532 nm. We also find that epitaxial films have an order of magnitude larger quantum efficiency at 650 nm than comparable polycrystalline films on Si. Additionally, these films permit angle-resolved photoemission spectroscopy measurements of the electronic structure, which are found to be in good agreement with theory. Epitaxial films open the door to dramatic brightness enhancements via increased efficiency near threshold, reduced surface disorder, and the possibility of engineering new photoemission functionality at the level of single atomic layers.

DOI: 10.1103/PhysRevLett.128.114801

Dense and coherent electron beams generated via photoemission have enabled many revolutionary tools in the physical sciences. These include x-ray-free electron lasers with 10^9 times higher peak x-ray brightness than previous sources [1,2], ultrafast electron microscopes that achieve femtosecond temporal and atomic structural resolution [3,4], hadron collider luminosity-enhancing systems based on electron beams [5], and next-generation electron linear colliders [6,7], which will probe physics beyond the standard model. Electron beam brightness, defined as the density of the beam in position-momentum phase space, is a central figure of merit for each of these applications [8]. According to Liouville's theorem, the brightness of any electron beam in a linear accelerator can be no greater than at its source [9,10]. Thus, the photoemission performance of photocathodes can determine the ultimate performance of accelerators ranging from meters to kilometers in length [11]. Photocathodes are also the critical enabling technology for many photon detectors, ranging from photomultipliers [12], image intensifiers, and ultrafast time-resolved streak cameras [13] to detectors for high-energy physics applications [14].

For intense beam generation or sensitive detection applications, many metallic photocathodes are infeasible choices due to their low quantum efficiencies (QEs)—the number of emitted electrons per incident photon. For metals, QEs generally range from 10^{-3} to 10^{-5} with ultraviolet illumination [15]. In contrast, the highest quantum efficiency materials, semiconductors containing or coated with alkali metals, have peak quantum efficiencies exceeding 1% in the visible region, with response extending into the near-infrared range [15]. In particular, the spectral response of alkali antimonides extends near the lasing wavelength of common high-bandwidth gain media and therefore can eliminate lossy wavelength conversion stages in both accelerator and detector applications [16–18]. Additionally, by limiting the required light intensity for a given photoelectron density, high quantum efficiency can mitigate multiphoton photoemission (MPPE). Since MPPE causes a dramatic increase in the momentum spread of photoelectrons, its suppression can dramatically improve beam brightness [19].

Owing to momentum conservation in the photoemission process, the transverse momentum spread of photoelectrons from clean, ordered, crystalline surfaces can be reduced by exploiting the material's band structure [20]. For single-crystal metal photocathodes, this has been theoretically modeled and experimentally verified [21,22]. Record low-momentum spread has been achieved in Cu (100) near the photoemission threshold; however, the efficiency ($\sim 10^{-8}$)

is too low for the beam current requirements of moderate- to high-intensity applications [22]. It is therefore desirable to synthesize maximally efficient cathodes as single-crystal films, where the smoothness, homogeneity, and termination can be controlled.

To date, all high-efficiency visible-light photocathodes are either grown as (often defect-rich) polycrystals or produced by activating a semiconductor surface (e.g., GaAs) with an alkali metal, commonly cesium, resulting in an intrinsically disordered emitter surface [23–25]. Owing to their alkali metal content, these photocathodes are extremely sensitive to vacuum contamination and cannot be characterized *ex situ*; a single Langmuir of oxygen is sufficient to alter their efficiency and surface chemistry [26–29]. While great progress has been made in the growth of alkali antimonide films using evaporative and sputtering techniques [30–35], smooth, epitaxial, single-phase samples remain elusive. This presents a barrier not only to the reduction of physical [36,37] and surface potential [38] roughness, but also to the engineering of these unique low-work-function semiconducting materials.

In this Letter, we demonstrate the first epitaxial growth of thin films of the high-efficiency photocathode material Cs_3Sb via molecular-beam epitaxy. The resulting films were characterized using a variety of *in situ* diagnostics including reflection high-energy electron diffraction (RHEED), x-ray and ultraviolet photoemission spectroscopy (XPS, UPS), and angle-resolved photoemission spectroscopy (ARPES). Structural and spectroscopic measurements of our films agree well with both previous studies of polycrystalline samples and density-functional theory (DFT) calculations of the electronic structure.

Cs_3Sb has a photoemission threshold > 600 nm, QE exceeding 1% at 530 nm, and crystallizes exclusively in a cubic structure with lattice constant a_{bulk} in the range of 9.14–9.19 Å [15,39–44]. Earlier work identified a $F_{d\bar{3}m}$ space group (NaTl-like) [39,41], while more recent studies favor an ordered $F_{m\bar{3}m}$ Cu_3Al structure [40,44]. The large cubic lattice constant presents a challenge in the selection of a suitable substrate; however, recent studies have identified 3C-SiC as a promising candidate due to its lattice parameter $a_{\mathrm{SiC}} = 4.36$ Å, nearly matching $a_{\mathrm{bulk}}/2 \approx 4.59$ (~5% strain), and the stability of its (001) surface [37,45].

Epitaxial thin films were grown on cubic 3C-SiC (001) substrates (epitaxial film on Si, MTI corporation) via MBE, using a sequence of shuttered growth of two unit cells (u.c.) at a substrate temperature of 40 °C and a recrystallization step at 85 °C. This process is described schematically in Fig. 1(a). During the growth phase, Sb is provided in eight doses of 1/4 nominal monolayers per SiC unit cell, separated by a 20 s pause, while Cs is provided continuously. The sample is then heated to the recrystallization temperature in vacuum, annealed in Cs flux for 15 min, and cooled in Cs flux back to the growth temperature. Each

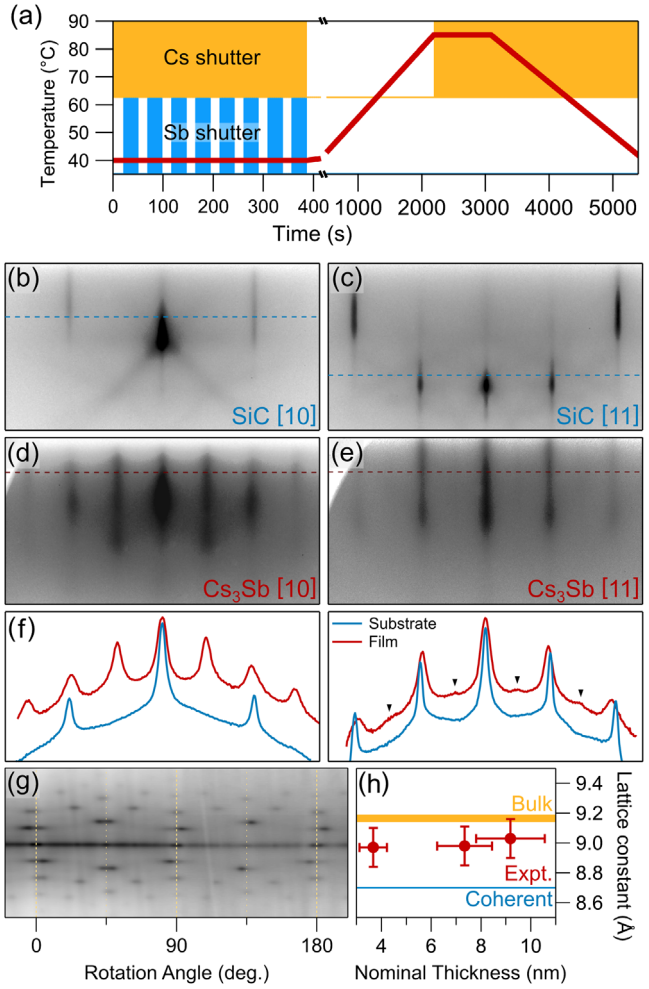

FIG. 1. Growth and structural characterization. (a) Substrate temperature (red line) and shutter states (filled areas, shutter open) during the growth and recrystallization process of 2 u.c. of (001)-oriented Cs_3Sb. RHEED images of an annealed SiC substrate (b),(c) and a 10 u.c. Cs_3Sb film (d),(e) along corresponding azimuths. (f) Line profiles of the substrate (blue) and film (red) along dashed lines in the above RHEED images (offset for clarity); half-order peaks are marked with black triangles. (g) RHEED line profile intensity of a 10 u.c. film as a function of the azimuthal angle (0° = [10], 45° = [11]). (h) In-plane lattice constant of three samples, measured using RHEED, grown under nominally identical conditions. Orange and blue lines mark the bulk Cs_3Sb lattice parameter and $2 \times a_{\mathrm{SiC}}$, respectively. A logarithmic intensity scale is used in (b)–(g).

cycle produces nominally 2 u.c. of Cs_3Sb, within the ±15% uncertainty of the quartz-crystal microbalance measurement of the Sb flux. This growth process departs from traditional codeposition procedures in favor of a solid-phase epitaxy approach as we have observed that films grown by codeposition at a single temperature are either crystalline or efficient photoemitters, but not both simultaneously. Films codeposited at low temperatures (< 80 °C) appear stoichiometric and have high QE, but lack ordered surfaces. Conversely, films codeposited at

higher temperatures (90 °C − 150 °C) form an ordered crystalline phase, but are generally Cs deficient (measured by XPS) and have low QE ($< 1 \times 10^{-4}$ at 532 nm). A low deposition temperature is necessary to reduce the Cs desorption rate and produce the correct stoichiometry; then the anneal is required to improve crystallinity and order the domains to produce an epitaxial film.

RHEED patterns of a SiC substrate and a 10 u.c. (nominally 9.2–9.5 nm) thick film are displayed in Fig. 1(b)–1(e). Comparison of the film diffraction patterns with the reciprocal lattice of Cs_3Sb confirm the cube-on-cube epitaxial relationship between film and substrate: $Cs_3Sb\langle 100\rangle // SiC\langle 100\rangle$. The in-plane ordering of the film is confirmed by a RHEED line profile intensity map presented in Fig. 1(g). This map shows both a 90° period, consistent with cubic symmetry, and no repetition of the Bragg peaks within a 45° window, precluding the presence of rotationally misaligned macroscopic domains. From the RHEED diffraction streak spacing, the in-plane lattice constant for the thinnest (4 u.c.) film is found to be $a_{\mathrm{film}} = 8.97 \pm 0.13$ Å, indicating partial relaxation ($2 \times a_{\mathrm{SiC}} < a_{\mathrm{film}} < a_{\mathrm{bulk}}$) at a thickness of only 3.8 nm. In Fig. 1(e), weak half-order streaks are present in the RHEED pattern along the [11] azimuth, evidenced by the line profiles in Fig. 1(f). These correspond to forbidden odd-index reflections in either the $F_{m\bar{3}m}$ or the $F_{d\bar{3}m}$ Cs_3Sb structure; their presence may signal the presence of lattice distortions (either intrinsic or induced by defects or vacancies) or a surface reconstruction.

To confirm the formation of the Cs_3Sb phase, *in situ* XPS measurements were performed and typical spectra are reported in Fig. 2. The dominant peaks in the Sb region correspond to the 3− valence, as expected for Cs_3Sb, while weak features corresponding to more oxidized species (1−, 3+) are also visible at higher binding energy. Between the Sb $3d_{3/2}$ and $3d_{5/2}$ peaks, weak peaks assigned to O 1*s* states of various Cs and Sb oxides are also visible, typical of Cs_3Sb that has been exposed to trace amounts of oxygen [26,28,29]. We attribute the surface oxidation to reaction with residual gasses in the UHV transfer system. The Cs $3d_{5/2}$ peak, Fig. 2(b), is shifted to slightly higher binding energy than the 1+ reference, attributed to band bending induced by surface oxidation [29], and is accompanied by a strong plasmon peak—typically correlated with high quantum efficiency [46,47]. Finally, valence band measurements, Fig. 2(c), agree with data on polycrystalline films reported in [46]. In particular, the Cs 5*s* to Cs 5*p* peak-area ratios closely match those reported by Bates *et al.* for high QE Cs_3Sb (attributed to minimal excess metallic Cs on the surface). We find area ratios ranging from 0.23 to 0.30 (or 0.15–0.21 if the Sb 4*d* tail contributions are subtracted) for samples with QE ranging from 2.1% to 3.3%.

Following growth, the QE of the samples was measured in an adjoining chamber using a biased collection coil.

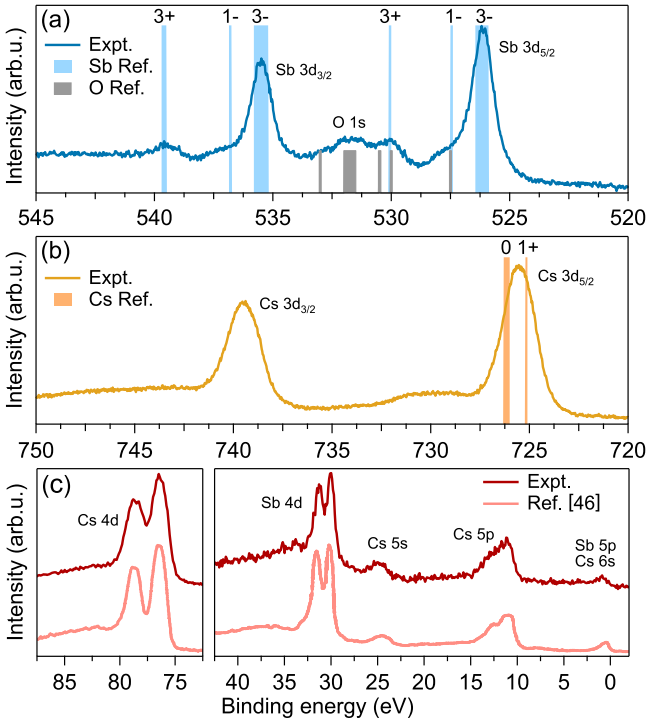

FIG. 2. XPS Spectra of a 7.4 nm thick epitaxial Cs_3Sb film. (a) Sb 3*d* and O 1*s* regions. Cyan bars indicate binding energy references for different Sb species; gray bars denote the O 1*s* references for different oxides. (b) Cs 3*d* region of the same sample. Orange bars indicate the literature references for the Cs oxidation states. (c) Valence band spectra including Cs 4*d*, 5*s*, 6*s*, and Sb 4*d* and 5*p* regions. Data from a high-efficiency polycrystalline Cs_3Sb film (reproduced from [46]) are provided for reference.

The QE of the ∼10 nm (10 u.c.) sample of Figs. 1(d) and 1(e) is shown in Fig. 3, demonstrating that its quantum efficiency exceeds 3% below 532 nm and is significantly enhanced at 650 nm (0.24%) compared to typical polycrystalline Cs_3Sb on silicon. In the inset, we report the QE (at 532 nm) of a sequentially grown thickness series; the QE exceeds 2% for the 4 u.c. sample and is not strongly affected by increasing thickness up to 9 nm. It is unlikely that the measured photocurrent includes electrons excited from the substrate since silicon carbide is a 2.3 eV indirect band gap semiconductor where direct optical transitions require photon energies exceeding 4 eV [48], well outside the measurement range. The measured thickness dependence departs from that of previous polycrystalline samples and represents an interesting avenue for future research.

Thickness is a critical parameter in determining a photocathode's response time—the resulting electron pulse length following illumination by a delta-function optical impulse. For semiconductor photocathodes, this is governed by the transit time of excited electrons to the surface [49] and is naturally restricted in thin samples. In our case, the electron transit time is expected to be on order ∼10 fs, based on our DFT-based *ab initio* photoemission

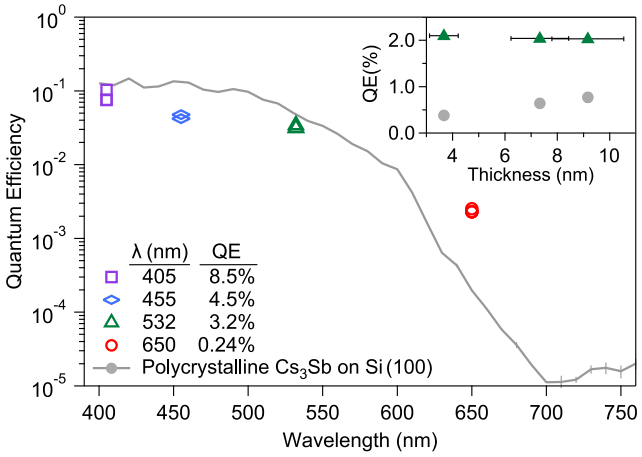

FIG. 3. Quantum efficiency, as a function of wavelength, for one sample, measured at two locations on the surface. The QE of a representative codeposited sample grown on Si (100) is included for comparison. Inset: the QE, at 532 nm, of three samples of varying thickness grown under the same nominal conditions (triangles) and the QE of the codeposited sample on Si whose spectral response is reported in the main figure (dots). The QE of a representative, codeposited, 116 ± 15 nm thick sample grown on Si (100) is included for comparison.

calculations. This suggests that these thin, epitaxial cathodes are excellent candidates for time-resolved electron beam instruments such as ultrafast microscopes [50] or high time-resolution streak cameras [13].

There is significant evidence that the electronic band structure, in concert with many-body effects, determines the momentum distribution of photoemitted electrons from atomically ordered surfaces, even when the photon energy is very near the photocathode work function [20–22,51,52]—where brightness is often largest [8,18]. Nonetheless, the minimum mean transverse energy measured in polycrystalline Cs_3Sb, ~20 meV at 90 K [53], is a factor of 2.6 larger than the free-electron thermal limit estimate [54] and an order of magnitude larger than the minimum predicted by our DFT-based *ab initio* photoemission theory [55]. Fully utilizing the electron band structure and maximizing photoemission brightness requires an atomically ordered surface [21,52,56], which has not been possible in alkali antimonides until now.

A major advantage of the epitaxial growth method presented here is that the resulting Cs_3Sb films possess sufficiently ordered surfaces such that the band structure is observed in the photoemitted electrons and can be measured using ARPES for comparison with theoretical calculations. Measurements were performed at room temperature in a background pressure of $P < 1 \times 10^{-10}$ torr using a helium plasma discharge lamp and the results are summarized in Fig. 4. Because of the highly three-dimensional nature of the band structure, determination of the out-of-plane momentum k_z is required to make quantitative comparisons to DFT calculations. We estimate the inner potential to be $V_0 = \phi + W$ [57] using the bandwidth $W \approx 1.2$ eV estimated from UPS spectra and the work function $\phi \approx 1.7$ eV measured from polycrystalline samples. This yields estimates of $k_z \approx 2.4$ and $k_z \approx 3.3$ Å^{-1} for He-I ($h\nu = 21.2$ eV) and He-II ($h\nu = 40.8$ eV), respectively. To assign the absolute momenta to positions in the Brillouin zone, in the presence of uncertainty in the out-of-plane lattice constant c_{film}, comparison of the ARPES spectra and DFT calculations is performed across several independent measurements (cf. Supplemental Material [58]). This gives a best fit with $k_z = 1.63$ reciprocal lattice units (r.l.u., where

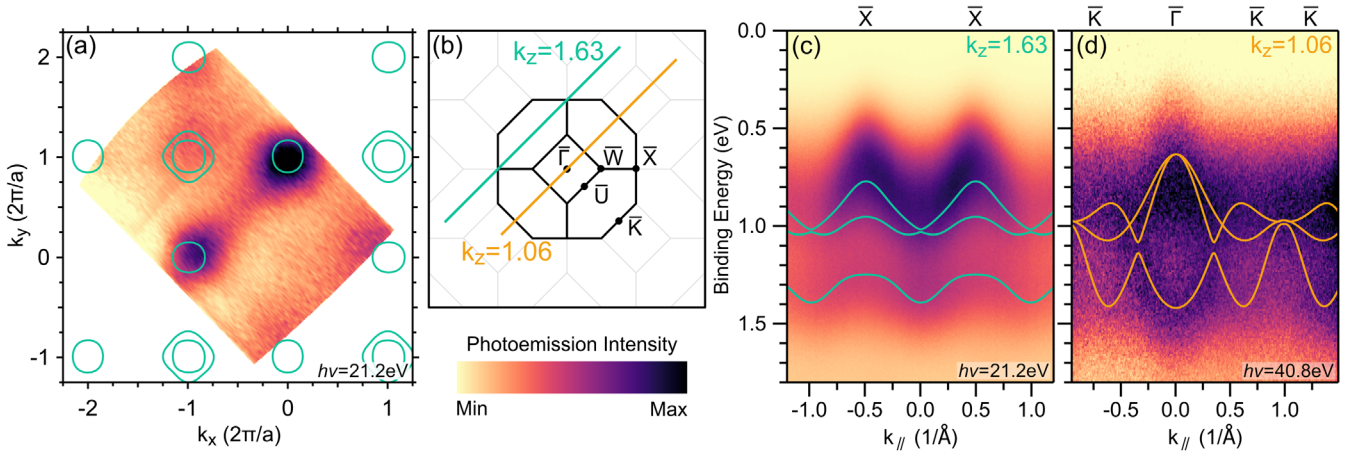

FIG. 4. *In situ* ARPES measurements of Cs_3Sb thin films. (a) Constant-energy intensity map integrated over a 50 meV window about $E - E_f = -0.55$ eV. Overlay (green) shows band positions at $E - E_{VBM} = -0.19$ eV calculated by DFT. (b) Schematic of the projected fcc Brillouin zone showing locations of the cuts shown in (c),(d). (c) ARPES spectrum passing through the edge of the projected zone at a nominal out-of-plane momentum of $k_z = 1.63$ r.l.u. Corresponding calculated band positions are shown in green. (d) Spectrum taken through the zone center at $k_z = 1.03$ r.l.u with calculated bands overlaid in orange. In (c),(d) the DFT bands have been offset in energy by −0.63 eV.

1 r.l.u. $= 2\pi/c_{\mathrm{film}}$) for He-I and $k_z = 1.06$ r.l.u. for He-II along with an overall shift of the Fermi level by 0.63 eV (attributable to pinning of E_f in the gap)—consistent with an inner potential of $V_0 = 3.2$ eV and lattice constant of $c_{\mathrm{film}} = 9.5$ Å.

Figure 4(a) shows a photoemission intensity map taken with He-I light at $E - E_f = 0.550$ eV, just cutting through the tops of the valence bands. The measured intensity pattern is consistent with a fcc Brillouin zone with $a_{\mathrm{film}} = 9.0$ Å. An overlay showing the calculated tops of the valence bands (at the same k_z and at an energy of $E - E_{VBM} = -0.190$ eV) agrees well with identified band positions. Figure 4(c) shows a cut along the $\bar{X} - \bar{X}$ direction taken with He-I light and Fig. 4(d) shows a cut along the $\bar{K} - \bar{\Gamma} - \bar{K}$ line taken with He-II. In the $\bar{X} - \bar{X}$ cut, we observe good agreement between the predicted and observed bands, with one brighter set between 0.5 and 1.0 eV of binding energy separated from a heavier and less intense band between 1.2 and 1.5 eV. In the $\bar{K} - \bar{\Gamma} - \bar{K}$ cut, we again observe a reasonable match between the predicted and observed dispersions—in particular, the holelike band at $\bar{\Gamma}$, at a k_z of 1.06 r.l.u., lies nominally at the X point of the fcc zone and constitutes the valence band maximum.

While there is good qualitative agreement with our calculations, we observe a roughly 10%–20% larger bandwidth in the ARPES spectra than is predicted by DFT. Preliminary calculations indicate that the Sb $3p$–Cs $6s$ bandwidth is influenced by the presence of both distortions from the ideal $F_{m\bar{3}m}$ structure and by biaxial compressive strain. The effects are found to be in competition, with distortions decreasing the bandwidth and strain increasing it, so we cannot disentangle their individual effects at present. This motivates further *in situ* structural characterization of this epitaxial phase, such as x-ray diffraction measurements [31–34] and a more detailed study of strain effects on the photoemission processes of Cs_3Sb.

In conclusion, we have used solid-phase epitaxy to grow (001)-oriented Cs_3Sb films on 3C-SiC (001) substrates. These films display unusually high efficiency at thicknesses as low as 4 u.c. (~3.8 nm). Thanks to the ordered nature of the sample surface, we have obtained the first ARPES measurements of the band structure, allowing direct comparison with DFT. As an indicator of what may be possible in the future, epitaxial control in other classes of semiconducting photocathodes has yielded remarkable new capabilities. Epitaxial strain induced in a GaAs/GaAsP superlattice lifts a band degeneracy at the valence band maximum and significantly enhances the spin polarization of the emitted electrons [82]. An even more intricate epitaxial layered structure enables an interferometric enhancement of absorption in GaAs, improving quantum efficiency by nearly an order of magnitude [83]. Control of the surface dipole moment in epitaxial GaN, an ultraviolet semiconductor photocathode, yields a negative electron affinity surface without cesium, greatly enhancing its intrinsic quantum efficiency and ease of use [84]. This Letter opens the door to similar engineering at the level of single atomic layers in the alkali antimonides: controlled doping, strain, termination, surface dipole moment, and heterostructuring are prime targets of future work for enhanced brightness in these remarkable photoemissive compounds.

The data that support the findings of this study are available within this Letter, Supplemental Material [58], and a data repository [85], including additional data related to the growth and structural characterization. Any additional data connected with the study are available from the corresponding author upon reasonable request.

This work was supported by the U.S. National Science Foundation Grants No. PHY-1549132, the Center for Bright Beams, DMR-2104427, and by the National Science Foundation [Platform for the Accelerated Realization, Analysis, and Discovery of Interface Materials (PARADIM)] under Cooperative Agreement No. DMR-2039380. This work made use of the Cornell Center for Materials Research Shared Facilities, which are supported through the NSF MRSEC program (DMR-1719875).

*C. T. P and A. G. contributed equally to this work.
†Corresponding author.
jmm586@cornell.edu

[1] P. Emma *et al.*, First lasing and operation of an Angstrom-wavelength free-electron laser, Nat. Photonics **4**, 641 (2010).
[2] M. Scholz, FEL performance achieved at European XFEL, *Proceedings of the 9th International Particle Accelerator Conference IPAC2018, Vancouver, Canada, International Particle Accelerator Conference* (JACoW Publishing, Geneva, 2018).
[3] V. A. Lobastov, R. Srinivasan, and A. H. Zewail, Four-dimensional ultrafast electron microscopy, Proc. Natl. Acad. Sci. U.S.A. **102**, 7069 (2005).
[4] G. Sciaini and R. J. D. Miller, Femtosecond electron diffraction: Heralding the era of atomically resolved dynamics, Rep. Prog. Phys. **74**, 096101 (2011).
[5] V. N. Litvinenko and Y. S. Derbenev, Coherent Electron Cooling, Phys. Rev. Lett. **102**, 114801 (2009).
[6] M. Bai *et al.*, C^3: A "cool" route to the Higgs boson and beyond, arXiv:2110.15800.
[7] S. Michizono, The international linear collider, Nat. Rev. Phys. **1**, 244 (2019).
[8] P. Musumeci, J. Giner Navarro, J. Rosenzweig, L. Cultrera, I. Bazarov, J. Maxson, S. Karkare, and H. Padmore, Advances in bright electron sources, Nucl. Instrum. Methods Phys. Res., Sect. A **907**, 209 (2018).
[9] I. V. Bazarov, B. M. Dunham, and C. K. Sinclair, Maximum Achievable Beam Brightness from Photoinjectors, Phys. Rev. Lett. **102**, 104801 (2009).
[10] D. Filippetto, P. Musumeci, M. Zolotorev, and G. Stupakov, Maximum current density and beam brightness achievable by laser-driven electron sources, Phys. Rev. ST Accel. Beams **17**, 024201 (2014).

[11] C. M. Pierce, M. B. Andorf, E. Lu, C. Gulliford, I. V. Bazarov, J. M. Maxson, M. Gordon, Y.-K. Kim, N. P. Norvell, B. M. Dunham, and T. O. Raubenheimer, Low intrinsic emittance in modern photoinjector brightness, Phys. Rev. ST Accel. Beams **23**, 070101 (2020).

[12] A. G. Wright, *The Photomultiplier Handbook* (Oxford University Press, New York, 2017).

[13] J. Liang, L. Zhu, and L. V. Wang, Single-shot real-time femtosecond imaging of temporal focusing, Light **7**, 42 (2018).

[14] A. Lyashenko, B. Adams, M. Aviles, T. Cremer, C. Ertley, M. Foley, M. Minot, M. Popecki, M. Stochaj, W. Worstell, J. Elam, A. Mane, O. W. Siegmund, H. Frisch, A. Elagin, E. Angelico, and E. Spieglan, Performance of large area picosecond photo-detectors (LAPPDTM), Nucl. Instrum. Methods Phys. Res., Sect. A **958**, 162834 (2020).

[15] A. Sommer, *Photoemissive Materials: Preparation, Properties, and Uses* (Krieger, New York, 1980).

[16] P. Musumeci, L. Cultrera, M. Ferrario, D. Filippetto, G. Gatti, M. S. Gutierrez, J. T. Moody, N. Moore, J. B. Rosenzweig, C. M. Scoby, G. Travish, and C. Vicario, Multiphoton Photoemission from a Copper Cathode Illuminated by Ultrashort Laser Pulses in an rf Photoinjector, Phys. Rev. Lett. **104**, 084801 (2010).

[17] L. Cultrera, C. Gulliford, A. Bartnik, H. Lee, and I. Bazarov, Ultra low emittance electron beams from multi-alkali antimonide photocathode operated with infrared light, Appl. Phys. Lett. **108**, 134105 (2016).

[18] J. Maxson, L. Cultrera, C. Gulliford, and I. Bazarov, Measurement of the tradeoff between intrinsic emittance and quantum efficiency from a NaKSb photocathode near threshold, Appl. Phys. Lett. **106**, 234102 (2015).

[19] J. K. Bae, I. Bazarov, P. Musumeci, S. Karkare, H. Padmore, and J. Maxson, Brightness of femtosecond nonequilibrium photoemission in metallic photocathodes at wavelengths near the photoemission threshold, J. Appl. Phys. **124**, 244903 (2018).

[20] B. L. Rickman, J. A. Berger, A. W. Nicholls, and W. A. Schroeder, Intrinsic Electron Beam Emittance from Metal Photocathodes: The Effect of the Electron Effective Mass, Phys. Rev. Lett. **111**, 237401 (2013).

[21] S. Karkare, W. Wan, J. Feng, T. C. Chiang, and H. A. Padmore, One-step model of photoemission from single-crystal surfaces, Phys. Rev. B **95**, 075439 (2017).

[22] S. Karkare, G. Adhikari, W. A. Schroeder, J. K. Nangoi, T. Arias, J. Maxson, and H. Padmore, Ultracold Electrons via Near-Threshold Photoemission from Single-Crystal Cu (100), Phys. Rev. Lett. **125**, 054801 (2020).

[23] T. Yamada, J. Fujii, and T. Mizoguchi, STM, STS, and local work function study of Cs/p-GaAs(110), Surf. Sci. **479**, 33 (2001).

[24] R. Fukuzoe, M. Hirao, D. Yamanaka, Y. Iwabuchi, H. Iijima, and T. Meguro, Preparation of Ga-terminated negative electron affinity-GaAs (100) surface by HCl-isopropanol treatment for nanoanalysis by scanning tunneling microscopy, J. Vac. Sci. Technol. B **36**, 06JK01 (2018).

[25] J. Biswas, J. Cen, M. Gaowei, O. Rahman, W. Liu, X. Tong, and E. Wang, Revisiting heat treatment and surface activation of GaAs photocathodes: In situ studies using scanning tunneling microscopy and photoelectron spectroscopy, J. Appl. Phys. **128**, 045308 (2020).

[26] C. W. Bates, T. M. van Atekum, G. K. Wertheim, D. N. E. Buchanan, and K. E. Clements, X-ray photoemission studies of superficially oxidized cesium antimonide photoemitters, Appl. Phys. Lett. **38**, 387 (1981).

[27] L. Danielson, C. Lee, and P. Oettinger, Laser illuminated high current photocathodes, Appl. Surf. Sci. **16**, 257 (1983).

[28] L. Soriano and L. Galán, Interaction of cesium-potassium antimonide photocathode materials with oxygen: An x-ray photoelectron spectroscopy study, Jpn. J. Appl. Phys. **32**, 4737 (1993).

[29] A. Galdi, W. J. I. DeBenedetti, J. Balajka, L. Cultrera, I. V. Bazarov, J. M. Maxson, and M. A. Hines, The effects of oxygen-induced phase segregation on the interfacial electronic structure and quantum efficiency of Cs_3Sb photocathodes, J. Chem. Phys. **153**, 144705 (2020).

[30] J. Feng, S. Karkare, J. Nasiatka, S. Schubert, J. Smedley, and H. Padmore, Near atomically smooth alkali antimonide photocathode thin films, J. Appl. Phys. **121**, 044904 (2017).

[31] M. Ruiz-Osés, S. Schubert, K. Attenkofer, I. Ben-Zvi, X. Liang, E. Muller, H. Padmore, T. Rao, T. Vecchione, J. Wong, J. Xie, and J. Smedley, Direct observation of bi-alkali antimonide photocathodes growth via in operando x-ray diffraction studies, APL Mater. **2**, 121101 (2014).

[32] S. Schubert, J. Wong, J. Feng, S. Karkare, H. Padmore, M. Ruiz-Osés, J. Smedley, E. Muller, Z. Ding, M. Gaowei, K. Attenkofer, X. Liang, J. Xie, and J. Kühn, Bi-alkali antimonide photocathode growth: An x-ray diffraction study, J. Appl. Phys. **120**, 035303 (2016).

[33] M. Gaowei, Z. Ding, S. Schubert, H. B. Bhandari, J. Sinsheimer, J. Kuehn, V. V. Nagarkar, M. S. J. Marshall, J. Walsh, E. M. Muller, K. Attenkofer, H. J. Frisch, H. Padmore, and J. Smedley, Synthesis and x-ray characterization of sputtered bi-alkali antimonide photocathodes, APL Mater. **5**, 116104 (2017).

[34] Z. Ding, M. Gaowei, J. Sinsheimer, J. Xie, S. Schubert, H. Padmore, E. Muller, and J. Smedley, In-situ synchrotron x-ray characterization of K_2CsSb photocathode grown by ternary co-evaporation, J. Appl. Phys. **121**, 055305 (2017).

[35] J. Xie, M. Demarteau, R. Wagner, S. Schubert, M. Gaowei, K. Attenkofer, J. Walsh, J. Smedley, J. Wong, J. Feng, H. Padmore, M. Ruiz-Oses, Z. Ding, X. Liang, E. Muller, and I. Ben-Zvi, Synchrotron x-ray study of a low roughness and high efficiency K_2CsSb photocathode during film growth, J. Phys. D **50**, 205303 (2017).

[36] J. Feng, S. Karkare, J. Nasiatka, S. Schubert, J. Smedley, and H. Padmore, Near atomically smooth alkali antimonide photocathode thin films, J. Appl. Phys. **121**, 044904 (2017).

[37] A. Galdi, J. Balajka, W. J. I. DeBenedetti, L. Cultrera, I. V. Bazarov, M. A. Hines, and J. M. Maxson, Reduction of surface roughness emittance of Cs_3Sb photocathodes grown via codeposition on single crystal substrates, Appl. Phys. Lett. **118**, 244101 (2021).

[38] S. Karkare and I. Bazarov, Effect of nanoscale surface roughness on transverse energy spread from GaAs photocathodes, Appl. Phys. Lett. **98**, 094104 (2011).

[39] K. H. Jack and M. M. Wachtel, The characterization and crystal structure of caesium antimonide, a photo-electric surface material, Proc. R. Soc. A **239**, 46 (1957).

[40] G. Gnutzmann, F. Wilhelm Dorn, and W. Klemm, Über einige A_3B- und AB_2-Verbindungen der schweren Alkalimetalle mit

Elementen der V. Gruppe, Z. Anorg. Allg. Chem. **309**, 210 (1961).
[41] W. H. McCarroll, Chemical and structural characteristics of the potassium-cesium-antimony photocathode, J. Phys. Chem. Solids **26**, 191 (1965).
[42] J. M. Barois, C. Fouassier, M. Onillon, and B. Tanguy, Experimental study of the non stoichiometry of cesium antimonide: Cs_3Sb, Mater. Chem. Phys. **24**, 189 (1989).
[43] J. Sangster and A. D. Pelton, The Cs-Sb (cesium-antimony) system, J. Phase Equilib. **18**, 382 (1997).
[44] J. C. Robbie and A. H. Beck, Scanning electron diffraction studies on caesium antimonide photocathodes during formation, J. Phys. D **6**, 1381 (1973).
[45] A. Galdi, C. T. Parzyck, W. J. I. DeBenedetti, J. Balajka, L. Cultrera, H. Paik, L. Moreschini, C. Hu, K. M. Shen, M. A. Hines, and J. M. Maxson, Understanding the growth dynamics Cs-Sb thin films via in-situ characterization techniques: Towards epitaxial alkali antimonide photocathodes, *Proceedings of the 12th International Particle Accelerator Conference (IPAC21), Campinas, Brazil* (JACoW Publishing, Geneva, 2021), pp. 2979–2982.
[46] C. W. Bates, D. Das Gupta, L. Galan, and D. N. Buchanan, x-ray photoemission studies of cesium antimonide photoemitters, Thin Solid Films **69**, 175 (1980).
[47] I. Martini, E. Chevallay, V. Fedosseev, C. Hessler, H. Neupert, V. Nistor, and M. Taborelli, X-ray photoemission spectroscopy studies of cesium antimonide photocathodes for photoinjector applications, Phys. Procedia **77**, 34 (2015).
[48] G. L. Zhao and D. Bagayoko, Electronic structure and charge transfer in 3C- and 4H-SiC, New J. Phys. **2**, 16 (2000).
[49] S. Karkare, L. Boulet, L. Cultrera, B. Dunham, X. Liu, W. Schaff, and I. Bazarov, Ultrabright and Ultrafast III–V Semiconductor Photocathodes, Phys. Rev. Lett. **112**, 097601 (2014).
[50] M. T. Hassan, J. S. Baskin, B. Liao, and A. H. Zewail, High-temporal-resolution electron microscopy for imaging ultrafast electron dynamics, Nat. Photonics **11**, 425 (2017).
[51] J. K. Nangoi, S. Karkare, R. Sundararaman, H. A. Padmore, and T. A. Arias, Importance of bulk excitations and coherent electron-photon-phonon scattering in photoemission from PbTe(111): Ab initio theory with experimental comparisons, Phys. Rev. B **104**, 115132 (2021).
[52] S. Karkare, J. Feng, X. Chen, W. Wan, F. J. Palomares, T.-C. Chiang, and H. A. Padmore, Reduction of Intrinsic Electron Emittance from Photocathodes Using Ordered Crystalline Surfaces, Phys. Rev. Lett. **118**, 164802 (2017).
[53] L. Cultrera, S. Karkare, H. Lee, X. Liu, I. Bazarov, and B. Dunham, Cold electron beams from cryocooled, alkali antimonide photocathodes, Phys. Rev. ST Accel. Beams **18**, 113401 (2015).
[54] J. Feng, J. Nasiatka, W. Wan, S. Karkare, J. Smedley, and H. A. Padmore, Thermal limit to the intrinsic emittance from metal photocathodes, Appl. Phys. Lett. **107**, 134101 (2015).
[55] J. K. Nangoi, S. Karkare, R. Sundararaman, G. Dodanduwa Waduge, J. K. Bae, A. Galdi, L. Cultrera, J. M. Maxson, I. V. Bazarov, H. A. Padmore, and T. A. Arias, Ab initio many-body calculations of the mean transverse energy for proposed high-brightness photocathode materials, in *The 5th Photocathode Physics for Photoinjectors Workshop Santa Fe, New Mexico, 2018*.
[56] G. S. Gevorkyan, S. Karkare, S. Emamian, I. V. Bazarov, and H. A. Padmore, Effects of physical and chemical surface roughness on the brightness of electron beams from photocathodes, Phys. Rev. ST Accel. Beams **21**, 093401 (2018).
[57] A. Damascelli, Probing the electronic structure of complex systems by ARPES, Phys. Scr. T **T109**, 61 (2004), 0307085.
[58] See Supplemental Material at http://link.aps.org/supplemental/10.1103/PhysRevLett.128.114801 for additional details and discussion concerning the growth optimization and DFT calculations as well as additional XPS, UPS, and ARPES spectra, which includes Refs. [59–81].
[59] R. E. Honig and D. A. Kramer, Vapor pressure data for the solid and liquid elements, RCA Rev. **30**, 285 (1969).
[60] D. Du, P. J. Strohbeen, H. Paik, C. Zhang, K. T. Genser, K. M. Rabe, P. M. Voyles, D. G. Schlom, and J. K. Kawasaki, Control of polymorphism during epitaxial growth of hyperferroelectric candidate LiZnSb on GaSb (111)B, J. Vac. Sci. Technol. B **38**, 022208 (2020).
[61] M. Schlipf and F. Gygi, Optimization algorithm for the generation of ONCV pseudopotentials, Comput. Phys. Commun. **196**, 36 (2015).
[62] R. Sundararaman, K. Letchworth-Weaver, K. A. Schwarz, D. Gunceler, Y. Ozhabes, and T. Arias, JDFTx: Software for joint density-functional theory, SoftwareX **6**, 278 (2017).
[63] N. Marzari, A. A. Mostofi, J. R. Yates, I. Souza, and D. Vanderbilt, Maximally localized Wannier functions: Theory and applications, Rev. Mod. Phys. **84**, 1419 (2012).
[64] N. Marzari and D. Vanderbilt, Maximally localized generalized Wannier functions for composite energy bands, Phys. Rev. B **56**, 12847 (1997).
[65] J. P. Perdew, K. Burke, and M. Ernzerhof, Generalized Gradient Approximation Made Simple, Phys. Rev. Lett. **77**, 3865 (1996).
[66] S. H. Wei and A. Zunger, Electronic structure of M_3ISb-type filled tetrahedral semiconductors, Phys. Rev. B **35**, 3952 (1987).
[67] A. R. Ettema and R. A. de Groot, Electronic structure of Cs_2KSb and K_2CsSb, Phys. Rev. B **66**, 115102 (2002).
[68] L. Kalarasse, B. Bennecer, and F. Kalarasse, Optical properties of the alkali antimonide semiconductors Cs_3Sb, Cs_2KSb, CsK_2Sb and K_3Sb, J. Phys. Chem. Solids **71**, 314 (2010).
[69] C. Cocchi and H. D. Saßnick, *Ab initio* quantum-mechanical predictions of semiconducting photocathode materials, Micromachines **12**, 1002 (2021).
[70] H.-D. Saßnick and C. Cocchi, Electronic structure of cesium-based photocathode materials from density functional theory: Performance of PBE, SCAN, and HSE06 functionals, Electronic structure and magnetism of inorganic compounds **3**, 027001 (2021).
[71] J. F. Moulder, W. F. Stickle, P. E. Sobol, and K. D. Bomben, *Handbook of X-ray Photoelectron Spectroscopy* (Perkin-Elmer Corporation, Eden Prairie, 1992).
[72] J. Yeh and I. Lindau, Atomic subshell photoionization cross sections and asymmetry parameters: $1 \leq Z \leq 103$, At. Data Nucl. Data Tables **32**, 1 (1985).
[73] M. A. H. Schmeißer, S. Mistry, H. Kirschner, S. Schubert, A. Jankowiak, T. Kamps, and J. Kühn, Towards the operation of Cs-K-Sb photocathodes in superconducting rf photoinjectors, Phys. Rev. ST Accel. Beams **21**, 113401 (2018).

[74] C. D. Wagner, Chemical shifts of Auger lines, and the Auger parameter, Faraday Discuss. Chem. Soc. **60**, 291 (1975).
[75] W. E. Morgan, W. J. Stec, and J. R. Van Wazer, Inner-orbital binding-energy shifts of antimony and bismuth compounds, Inorg. Chem. **12**, 953 (1973).
[76] J. Jupille, P. Dolle, and M. Besançon, Ionic oxygen species formed in the presence of lithium, potassium and cesium, Surf. Sci. **260**, 271 (1992).
[77] S. J. Yang and C. W. Bates, The role of cesium suboxides in low-work-function surface layers studied by x-ray photoelectron spectroscopy: Ag-O-Cs, Appl. Phys. Lett. **36**, 675 (1980).
[78] C. D. Wagner, D. A. Zatko, and R. H. Raymond, Use of the oxygen KLL Auger lines in identification of surface chemical states by electron spectroscopy for chemical analysis, Anal. Chem. **52**, 1445 (1980).
[79] N. G. Krishnan, W. N. Delgass, and W. D. Robertson, Electron binding energies of core levels in caesium adsorbed on a nickel (100) surface, J. Phys. F **7**, 2623 (1977).
[80] G. Ebbinghaus and A. Simon, Electronics structures of Rb, Cs and some of their metallic oxides studied by photoelectron spectroscopy, Chem. Phys. **43**, 117 (1979).
[81] K. Momma and F. Izumi, VESTA3 for three-dimensional visualization of crystal, volumetric and morphology data, J. Appl. Crystallogr. **44**, 1272 (2011).
[82] T. Maruyama, D.-A. Luh, A. Brachmann, J. E. Clendenin, E. L. Garwin, S. Harvey, J. Jiang, R. E. Kirby, C. Y. Prescott, R. Prepost, and A. M. Moy, Systematic study of polarized electron emission from strained GaAs/GaAsP superlattice photocathodes, Appl. Phys. Lett. **85**, 2640 (2004).
[83] W. Liu, Y. Chen, W. Lu, A. Moy, M. Poelker, M. Stutzman, and S. Zhang, Record-level quantum efficiency from a high polarization strained GaAs/GaAsP superlattice photocathode with distributed Bragg reflector, Appl. Phys. Lett. **109**, 252104 (2016).
[84] J. Marini, I. Mahaboob, E. Rocco, L. D. Bell, and F. Shahedipour-Sandvik, Polarization engineered *N*-polar Cs-free GaN photocathodes, J. Appl. Phys. **124**, 113101 (2018).
[85] A repository at https://doi.org/10.34863/6d5f-aj24 contains detailed growth parameters, as well as XPS and ARPES characterization data, for the samples prepared and measured in the course of this investigation.

Supplementary Information for: A single crystal alkali antimonide photocathode: high efficiency in the ultra-thin limit

C. T. Parzyck,[1] A. Galdi,[2] J. K. Nangoi,[1] W. J. I. DeBenedetti,[3] J. Balajka,[3] B. D. Faeth,[4] H. Paik,[4] C. Hu,[1] T. A. Arias,[1] M. A. Hines,[3] D. G. Schlom,[5,6,7] K. M. Shen,[1,6] and J. M. Maxson[2]

[1] *Laboratory of Atomic and Solid State Physics, Department of Physics, Cornell University, Ithaca, NY 14853, USA*
[2] *Cornell Laboratory for Accelerator-Based Sciences and Education, Cornell University, Ithaca, NY 14853, USA*
[3] *Department of Chemistry and Chemical Biology, Cornell University, Ithaca, NY 14853, USA*
[4] *Platform for the Accelerated Realization, Analysis, and Discovery of Interface Materials (PARADIM), Cornell University, Ithaca, NY 14853, USA*
[5] *Department of Materials Science and Engineering, Cornell University, Ithaca, NY 14853, USA*
[6] *Kavli Institute at Cornell for Nanoscale Science, Cornell University, Ithaca, NY 14853, USA*
[7] *Leibniz-Institut für Kristallzüchtung, Max-Born-Straße 2, 12489 Berlin, Germany*

(Dated: December 29, 2021)

CONTENTS

SAMPLE GROWTH AND STRUCTURAL CHARACTERIZATION

Cs_3Sb thin films were grown on 10 mm×10 mm SiC substrates affixed to custom niobium sample holders and grounded using a silver paste (PELCO No. 16047). The substrates were sonicated in acetone and isopropyl alcohol, rinsed with deionized water, and vacuum annealed in the growth chamber at 650 °C for 15 minutes prior to growth until a clear electron diffraction pattern was observed. Substrates were heated to the desired temperature using a resistive heater and the temperature was monitored using a thermocouple located behind the sample holder. Films were grown using molecular beams from an elemental Sb source (Alfa/AESAR, 99.9999%) and a cesium (Alfa/AESAR 99.98%) indium (Alfa/AESAR, 99.9999+%) alloy source containing about 80 at% indium. This alloy was melted and subsequently solidified in a glove box, after which exposure to air for loading into the MBE was possible. The vapor pressure of indium is about 10 orders of magnitude lower than that of cesium [1], making such an alloy a convenient way to provide a pure molecular beam of cesium in a way that can be loaded into the MBE in air [2]. Typical fluxes for the sources were $(4.2-4.9)\times10^{12}$ atoms/cm^2/s for Sb and $(4-5)\times10^{13}$ atoms/cm^2/s for Cs as determined by the flux measured with a quartz crystal microbalance (QCM), with an accuracy of ±15%.

As discussed in the main text, a two-step deposition/crystallization procedure was required to produce samples that were both epitaxial and possessing high quantum efficiency. For comparison, RHEED patterns of samples grown under different conditions are provided in Fig. S1. Panels (a-b) show the RHEED patterns of samples grown at a fixed, low temperature using the traditional codeposition procedure; the sample in Fig. S1(a) has the highest quantum efficiency of the batch described here (7% at 532 nm) but suffers from poor crystallinity and a rough surface—evidenced by the large incoherent background, presence of polycrystalline rings/spots, and the strong vertical modulation of the primary RHEED streaks. Adding a higher temperature anneal following codeposition substantially improves the crystallinity, as shown in the RHEED images in Fig. S1(c). We note, however, that once a thick layer (*e.g.,* 30 u.c.) is grown even a high temperature anneal cannot fully convert a partially polycrystalline or fiber texture sample to a fully epitaxial one. This is apparent in the remaining polycrystalline spots in Fig. S1(d) and horizontal lines connecting

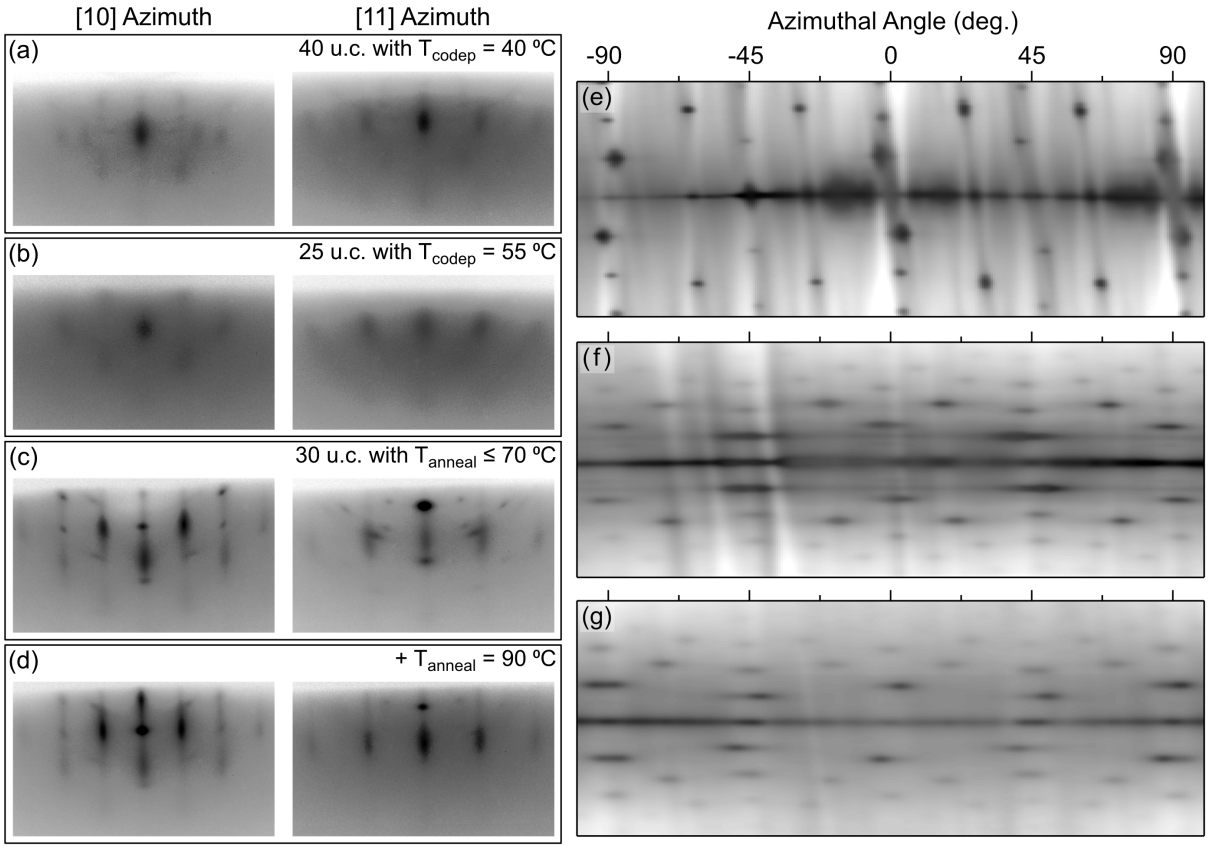

FIG. S1. Effects of deposition and annealing temperature on sample growth. Panels (a-b) show RHEED patterns of samples produced by codeposition at a fixed temperature. Panel (c) shows the RHEED pattern of a sample grown by the two-step process discussed in the main text, but with lower annealing temperatures (60-70 °C). Panel (d) shows the same sample, but after an additional 90 °C anneal. Panels (e-g) are line profile intensities of RHEED patterns as a function of the azimuthal angle. The vertical axis of the map is the horizontal coordinate on the screen; the horizontal axis is the rotation angle about the sample normal. A typical SiC substrate pattern is shown in (e) and the same film as pictured in panel (d) is shown here in (f). Panel (g) is from a sample grown under optimized conditions and is the same as in Fig. 1(g) of the main text. All panels use a logarithmic intensity scale.

the Bragg peaks in Fig. S1(f). These horizontal lines signal the presence of rotationally misaligned domains and are not present in the substrate RHEED, Fig. S1(e), or in a fully epitaxial film, Fig. S1(g).

In Fig. S2(a-b), we report the RHEED patterns of one of the epitaxial samples collected at angles corresponding to the [10] and [11] azimuths of the substrate RHEED pattern. In particular, for the sample of Fig. S2 (a-b), the streaks in the pattern appear modulated, as a consequence of a multi-stepped surface, with intensity maxima corresponding to the 3D reciprocal space lattice points. The patterns are compared with the projection of the reciprocal lattice of the $F_{d\bar{3}m}$ structure with [100] (in (a)) and and [110] (in (b)) zone axis, confirming the cube-on-cube epitaxial relationship between film and substrate (SiC $\langle 100 \rangle$ || Cs_3Sb $\langle 100 \rangle$). Both the ordered, lower symmetry $F_{m\bar{3}m}$ structure, shown in Fig. S2(c), and the disordered $F_{d\bar{3}m}$ structure, Fig. S2(b), are compatible with the measured RHEED patterns.

The weak half-period streaks, visible in Fig. S2(b), correspond to diffraction peaks normally forbidden by the FCC structure factor. Based on simulated electron diffraction patterns, even small distortions from the ideal structure are expected to generate weak half-order streaks. Such distortions may be intrinsic, as observed in DFT calculations, or may be induced by periodic dislocations or vacancies. Another possibility is the presence of a surface reconstruction, possibly coincident with a slightly different stoichiometry at the sample surface [4].

DENSITY FUNCTIONAL THEORY CALCULATIONS

The electronic structure calculations of Cs_3Sb presented here employ the plane-wave density-functional theory (DFT) framework with the GGA-PBE exchange-correlation functional [5] and SG15 norm-conserving pseudopotentials

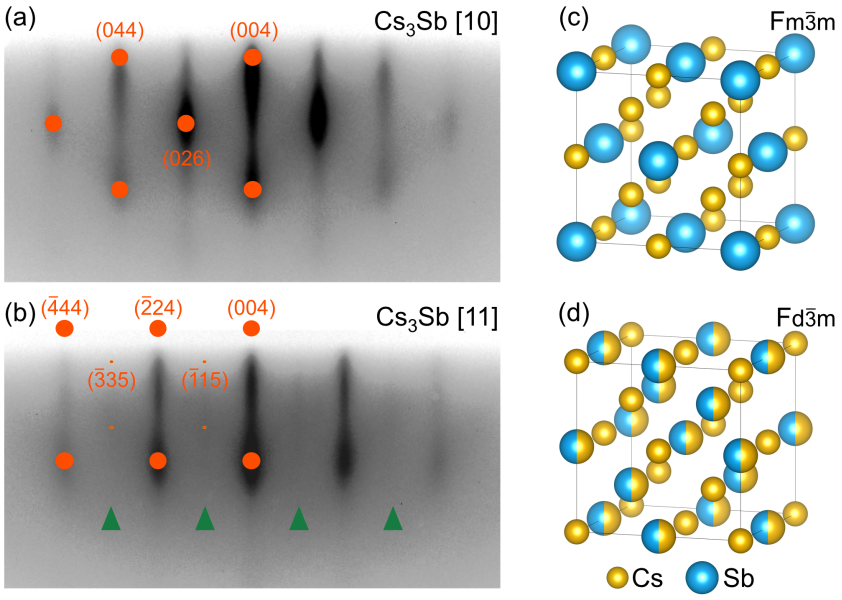

FIG. S2. (a-b) Additional RHEED images (logarithmic intensity scale) of a typical epitaxial Cs_3Sb sample. Orange dots represent the reciprocal lattice points of Cs_3Sb with $F_{d\bar{3}m}$ structure with size proportional to the structure factor calculated using the ion electronic charge Z as atomic form factor. In (a) the reciprocal lattice is plotted about the [100] zone axis and in (b) about the [110] zone axis. Green arrows in (b) indicate the position of weak streaks corresponding to odd-index reflections. The Cs_3Sb unit cells with $F_{m\bar{3}m}$ and $F_{d\bar{3}m}$ structure are shown in (c) and (d), respectively [3].

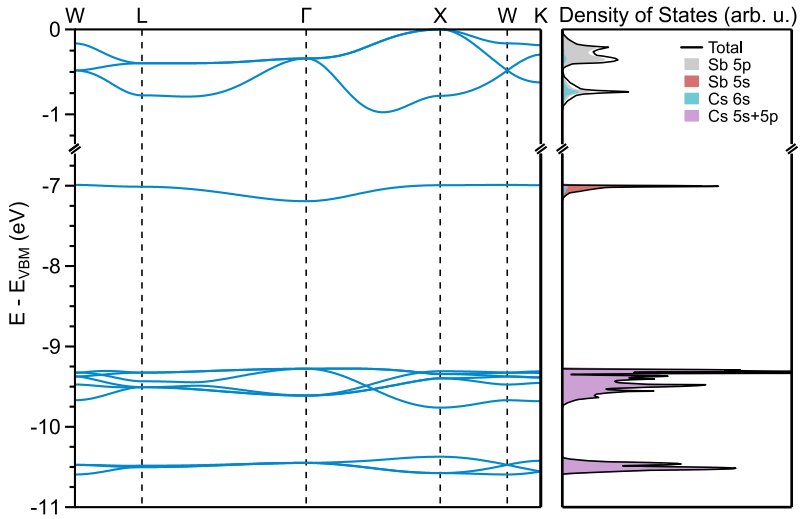

FIG. S3. DFT calculations of the $F_{m\bar{3}m}$ structure of Cs_3Sb along with the orbital projected density of states.

[6] as implemented in JDFTx [7], a face-centerd-cubic (FCC) primitive cell, a plane-wave cutoff of 40 Hartrees, and an optimized lattice constant of 9.40 Å. The calculations of total ground state energy and density of states employ a Brillouin zone sampling mesh of 4x4x4. For simplified comparison with the ARPES spectra we utilize the Wannier interpolation technique [8] to generate a maximally localized Wannier basis set [9] using a supercell of 4x4x4 fcc primitive cells and using linear combinations of bulk Bloch bands at energies from 11 eV below to the valence band maximum. This Wannier basis set reproduces the bulk bands of the $F_{m\bar{3}m}$ structure well and is shown in Fig. S3. As expected, the near E_f manifold is composed primarily of Sb $5p$ and Cs $6s$ states and the DOS is split into two distinct peaks, which are reflected in the valence bands shown in Fig S6. DFT calculations of the band structure presented here match well previous investigations, though the optimized lattice constant used here ($a_{cubic} = 9.40$ Å) deviates from the experimental value. This is not unexpected given the sensitivity of the theoretical lattice constant

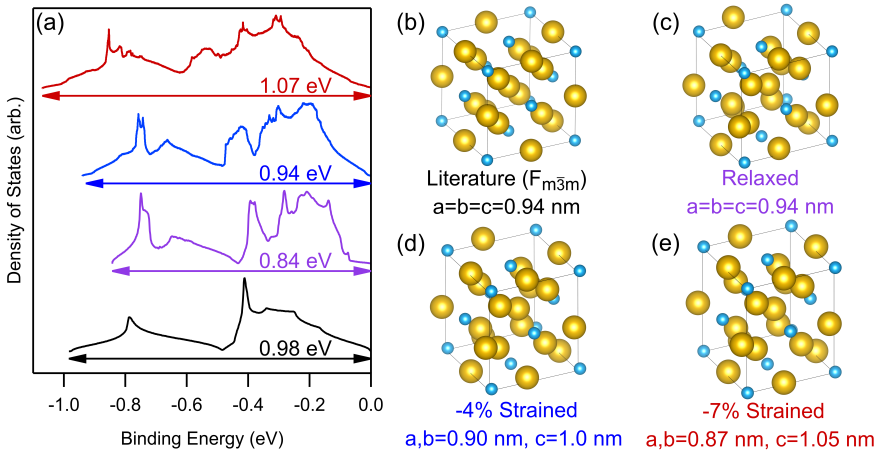

FIG. S4. (a) Total density of states for various structures of Cs_3Sb. The DOS of the literature $F_{m\bar{3}m}$ structure (b) is in black, the relaxed cubic structure (c) is in purple, an in-plane compressive strain of 4% (d) is in blue, and a compressive strain of 7% (e) in red.

to choice of calculation framework (DFT, GW) and specifics of the calculation (e.g. the choice of exchange-correlation functional). As such, theoretical predictions of the lattice constant vary from 8.920 Å to 9.415 Å in the literature [10–14]. For the purposes of comparison with the experimental data presented in the main text and Fig S7 we have used the band structure from the literature $F_{m\bar{3}m}$ structure and re-scaled the momenta to reflect the measured lattice constant of 9.0 Å. As our electron diffraction images suggest some degree of in-plane compressive strain we estimate the effects of strain on the out-of-plane lattice constant. From a set of relaxation calculations we find the relationship

$$\frac{c}{a_{bulk}} \approx 1 + 2.85\ \frac{a_{bulk} - a}{a_{bulk}}. \tag{1}$$

Assuming a 2% strain from a bulk lattice constant of $a_{bulk} = 9.18$Å we can estimate $c \approx 9.56$ Å.

Finally, we have investigated the effects of distortion and strain on the electronic structure of Cs_3Sb and some preliminary results are detailed in Fig. S4. First, we find that when viewed in a larger simple cubic cell the FCC structure is not stable and relaxation calculations suggest the presence of distortions from the $F_{m\bar{3}m}$ structure, depicted in (c). The inclusion of these distortions appear to reduce the Sb 5p/Cs 6s bandwidth by $\sim 14\%$. However, the additional application of an in-plane compressive stress of $\sim 4\%$ returns the bandwidth to around that of the FCC structure, and a further strain of $\sim 7\%$ increases the bandwidth to about $\sim 9\%$ above the literature prediction. As noted in the main text, the ARPES band structure, Fig. S8, appears to have a bandwidth roughly 10 to 20% larger then predicted by the literature calculation of Fig. S3. Similarly, the UPS spectra in Fig. S6 yield a total bandwidth of 1.2 ± 0.18 for the Sb $5p$/Cs $6s$ manifold. Both of these (and the half order diffraction peaks in Fig. S2) are consistent with some combination of strain and distortion, but the relative contributions cannot, at present, be disentangled.

PHOTOEMISSION MEASUREMENTS

In situ photoemission measurements were conducted by transferring the samples through an ultra high vacuum manifold ($P < 2 \times 10^{-9}$ Torr) to a measurement chamber immediately following film growth. Angle Resolved Photoemission Spectroscopy (ARPES) measurements were performed using a Scienta Omicron DA30-L electron analyzer equipped with a Fermion Instruments BL1200s Helium discharge lamp to produce Helium-I ($h\nu = 21.2$ eV) and Helium-II ($h\nu = 40.8$ eV) light. Measurements were performed at room temperature at a pass energy of 10 eV, with nominal system energy and angular resolutions of 20 meV and 0.4°, respectively. X-ray photoemission spectroscopy (XPS) measurements were conducted in the same system using a Scienta Omicron DSX400 x-ray source with a Mg anode ($h\nu = 1253.6$ eV) at a pass energy of 100 eV and nominal energy resolution of 0.375 eV. The base pressure in the ARPES system is better than 5×10^{-11} Torr and during measurements the pressure was maintained between 9×10^{-11} and 3×10^{-10} Torr.

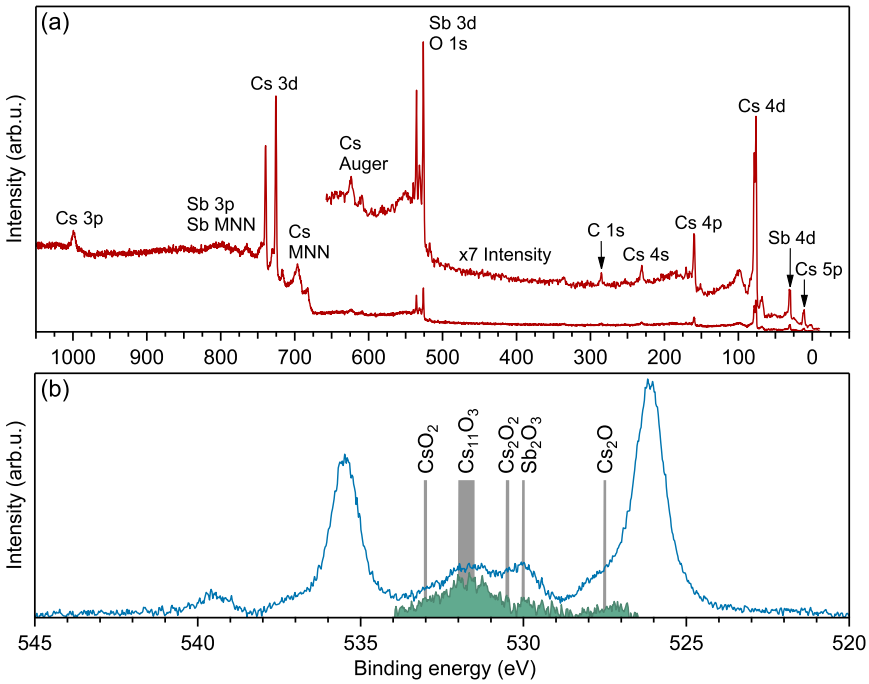

FIG. S5. (a) Typical XPS survey spectrum of a Cs_3Sb sample measured with Mg Kα radiation; peaks are labeled following ref.[15]. (b) Background subtracted Sb 3d and O 1s region. The O 1s contribution, isolated from the Sb one, is shown as a shaded area. Reference energies for several Cs and Sb oxides are marked with grey bars.

X-Ray Photoemission Spectroscopy

TABLE S1. Energy references found in literature with corresponding valence state for Sb $3d_{5/2}$, O 1s and Cs $3d_{5/2}$. The Sb $3d_{3/2}$ energy can be obtained by adding the spin-orbit coupling energy of 9.355 eV. "This work" indicates the binding energies we obtained from our reference samples (metallic Sb and CsSb).

Peak	valence	compound	ref.BE (eV)	source
Sb $3d_{5/2}$	3-	Cs-Sb/Cs-K-Sb	525.9-526.45	16–18
Sb $3d_{5/2}$	1−	CsSb	527.45	This work
Sb $3d_{5/2}$	0	Sb	528.3	This work
Sb $3d_{5/2}$	3+	Sb_2O_3	530-530.1	19 and 20
O 1s	2−	Cs_2O	527.5	21 and 22
O 1s	2−	Sb_2O_3	530.0	23
O 1s	1−	Cs_2O_2	530.5	21
O 1s	2−	$Cs_{11}O_3$	531.5-532.1	16 and 22
O 1s	1/2−	CsO_2	533	21
Cs $3d_{5/2}$	0	Cs	726.0-726.3	24 and 25
Cs $3d_{5/2}$	1+	Cs_2O	725.1-725.2	22 and 25

A typical XPS survey spectrum is reported in Fig. S5 (a); in (b) we report a typical Sb 3d-O 1s spectrum after subtraction of a Tougaard background. The oxygen contribution has been isolated from the total spectrum as shown in [26], and the peak position compared to the literature energy references reported in Table S1. The dominant oxygen peak corresponds to Cs suboxides, usually referred to as $Cs_{11}O_3$, as typically observed in the first stages of oxidation of Cs-containing alkali antimonide films [16, 26].

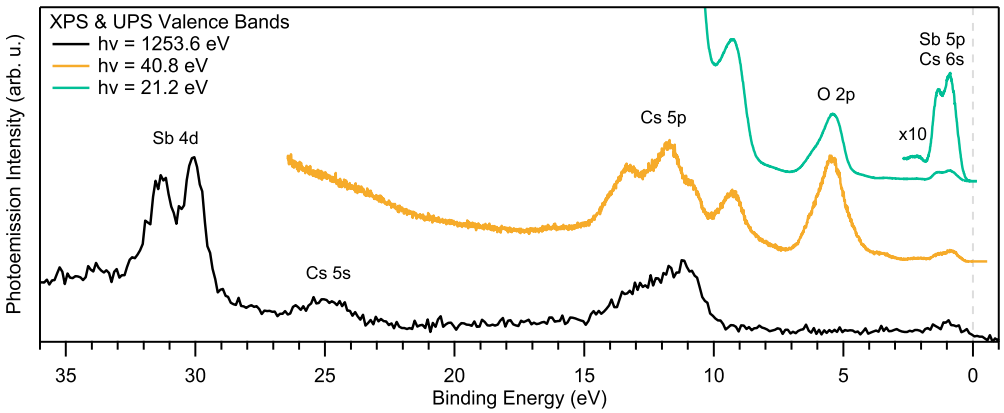

FIG. S6. Valence bands of Cs_3Sb films collected using Mg Kα (black), Helium II (yellow), and Helium I (green) radiation. Traces have been re-scaled and offset for clarity.

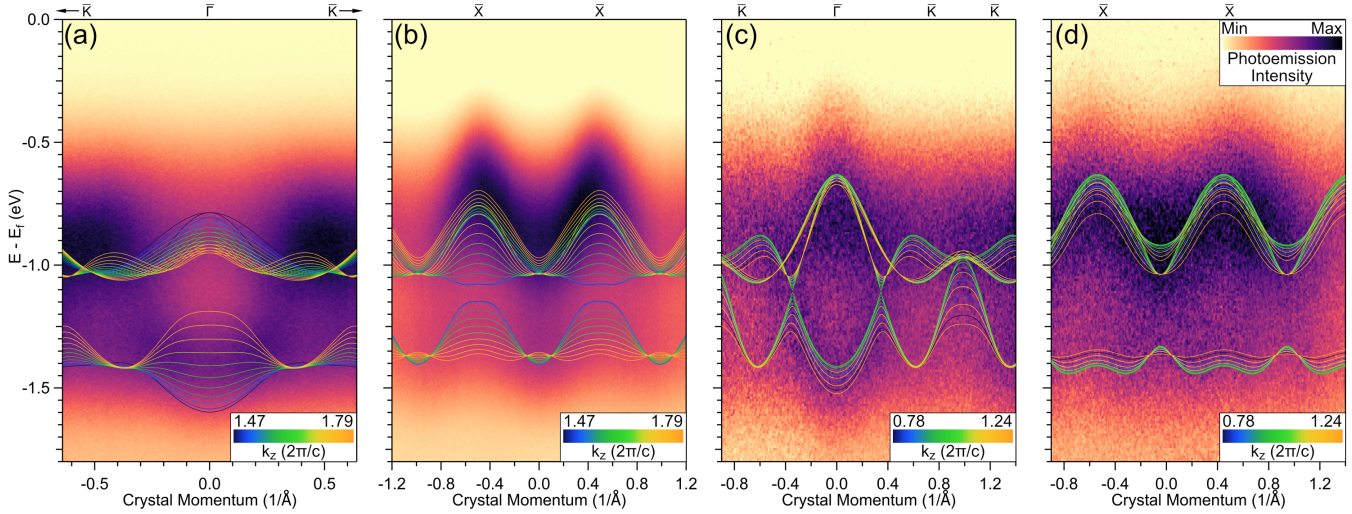

FIG. S7. DFT overlays for ARPES measurements along high symmetry lines in the projected FCC zone. Data in panels (a-b) were taken with $h\nu = 21.2$ eV light and data in panels (c-d) were taken using $h\nu = 40.8$ eV light.

Ultraviolet Photoemission Spectroscopy

Angle integrated photoemission spectra of the valence bands of epitaxial Cs_3Sb films are presented in Fig. S6. At higher binding energies the Sb 4d and Cs 5s peaks are visible using x-ray radiation, and the area ratios of these peaks are found to be in good agreement with previous literature studies of high efficiency photoemitters [4]. To understand the structure of the lower binding energy peaks between 0 and 15 eV it is important to take into account the photoemission cross sections of the various orbitals, as tabulated by Yeh and Lindau [27]. For simplicity we can examine the cross sections relative to the Sb 5p cross section σ_{Sb5p} which is 2.6 Mb at 21.2 eV, 2.9×10^{-1} at 40.8 eV, and 2.1×10^{-3} at 1253.6 eV. At low energies, the oxygen 2p cross section is enhanced ($\sigma_{O2p}/\sigma_{Sb5p} \approx 4$ at 21.2eV and ≈ 24 at 40.8 eV) so that even a submonolayer coverage of oxide on the surface (*i.e.* $\lesssim 3$ O per 1 Sb) will produce a strong response in the UPS spectra, which is observed. At high photon energy, however, the oxygen cross section is suppressed below that of the antimony ($\sigma_{O2p}/\sigma_{Sb5p} \approx 0.2$ at 1253.6 eV) and the corresponding O $2p$ peaks are not visible.

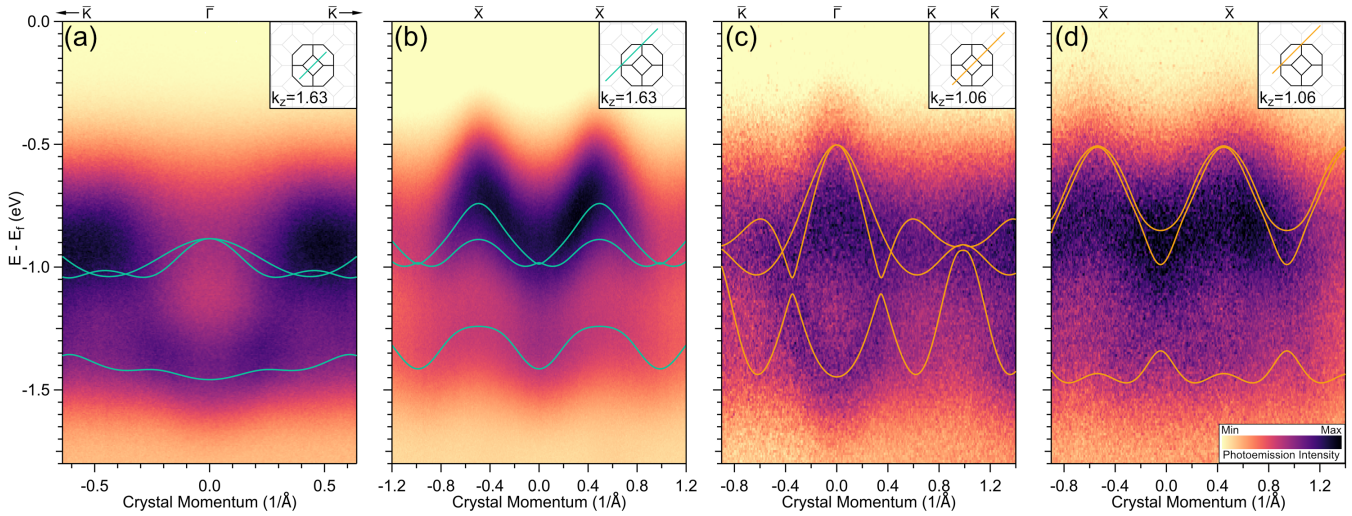

FIG. S8. Selected "best fit" DFT overlays from Fig. S7. Panels (a-b) do not correspond to particular high symmetry lines in the full FCC zone since $k_z \sim 1.63$ r.l.u. and $\bar{X} = X$ and $\bar{K} = K$ only when $k_z = 2n$ for $n \in \mathbb{Z}$. Panels (c-d) correspond to cuts nearly through the top of the zone since $\bar{\Gamma} = X$ when $k_z = 2n + 1$ for $n \in \mathbb{Z}$.

Angle Resolved Photoemission Spectroscopy

As discussed in the main text the highly three dimensional nature of the band structure presents a challenge when comparing the ARPES and DFT results. We can estimate the inner potential to be $V_0 \approx \phi + W$ where $\phi \approx 1.7$ eV is the work function and $W \approx 1.2$ eV is the bandwidth [28]. The out-of-plane momentum (in reciprocal lattice units) is then

$$k_z = \left(\frac{mc}{\pi\hbar}\right)\sqrt{E_{kin}\cos^2(\varphi) + V_0} \tag{2}$$

where $c \approx 9.56$ Å is the out-of-plane lattice constant, E_{kin} is the electron kinetic energy, and $\cos^2(\varphi) \approx 1$ for the range of angles emission angles, φ, used in the measurement geometry. Taking into account uncertainties in ϕ, W, and c we estimate $k_z \approx 3.63 \pm 0.17$ for He-I and $k_z \approx 5.01 \pm 0.23$ for He-II. For simplicity, these are folded back into the first and second FCC zones (*n.b.* in our convention the FCC zone spans from -1 to +1 r.l.u using the lattice constant corresponding to the conventional cubic unit cell) giving estimates of $k_z \approx 1.63$ r.l.u. and $k_z \approx 1.01$ r.l.u. for He-I and He-II, respectively. We then plot overlays for these confidence intervals in Fig. S7 and select a set that gives the best average agreement for all four cuts with one set of parameters. This chosen set has very similar values of k_z to the ones estimated above and are shown in Fig. S8. This set corresponds to a choice of $V_0 = 3.2$ eV and $c = 9.5$ Å, which are in good agreement with what is expected from the above arguments. An energy offset of 0.630 eV is used between the DFT valence band maximum and the measured Fermi energy, E_f, to place the DFT bands as centrally on the spectra in Fig. S7 and S8. Even doing so, however, the bandwidth of the measured ARPES spectra appears somewhat larger then the band positions from the calculations indicate, as is particularly obvious in panel Fig S8 (b). It is for this reason that in panel Fig. 4 (a) of the main text the DFT calculation in the overly is given at a slightly lower binding energy ($E - E_{VBM} = -0.19$ eV, $E - E_f = -0.82$ eV) then the corresponding ARPES data ($E - E_f = -0.55$ eV).

[1] R. E. Honig, Vapor pressure data for the solid and liquid elements, RCA review **30**, 285 (1969).
[2] D. Du, P. J. Strohbeen, H. Paik, C. Zhang, K. T. Genser, K. M. Rabe, P. M. Voyles, D. G. Schlom, and J. K. Kawasaki, Control of polymorphism during epitaxial growth of hyperferroelectric candidate LiZnSb on GaSb (111)B, Journal of Vacuum Science & Technology B **38**, 022208 (2020).
[3] K. Momma and F. Izumi, *VESTA3* for three-dimensional visualization of crystal, volumetric and morphology data, Journal of Applied Crystallography **44**, 1272 (2011).
[4] C. W. Bates, D. Das Gupta, L. Galan, and D. N. Buchanan, X-ray photoemission studies of cesium antimonide photoemitters, Thin Solid Films **69**, 175 (1980).
[5] J. P. Perdew, K. Burke, and M. Ernzerhof, Generalized Gradient Approximation Made Simple, Physical Review Letters **77**, 3865 (1996).
[6] M. Schlipf and F. Gygi, Optimization algorithm for the generation of ONCV pseudopotentials, Computer Physics Communications **196**, 36 (2015), 1502.00995.
[7] R. Sundararaman, K. Letchworth-Weaver, K. A. Schwarz, D. Gunceler, Y. Ozhabes, and T. Arias, JDFTx: Software for joint density-functional theory, SoftwareX **6**, 278 (2017).
[8] N. Marzari, A. A. Mostofi, J. R. Yates, I. Souza, and D. Vanderbilt, Maximally localized Wannier functions: Theory and applications, Reviews of Modern Physics **84**, 1419 (2012).
[9] N. Marzari and D. Vanderbilt, Maximally localized generalized Wannier functions for composite energy bands, Physical Review B **56**, 12847 (1997).
[10] S. H. Wei and A. Zunger, Electronic structure of M_3ISb-type filled tetrahedral semiconductors, Physical Review B **35**, 3952 (1987).
[11] A. R. Ettema and R. A. de Groot, Electronic structure of Cs_2KSb and K_2CsSb, Physical Review B - Condensed Matter and Materials Physics **66**, 1151021 (2002).
[12] L. Kalarasse, B. Bennecer, and F. Kalarasse, Optical properties of the alkali antimonide semiconductors Cs_3Sb, Cs_2KSb, CsK_2Sb and K_3Sb, Journal of Physics and Chemistry of Solids **71**, 314 (2010).
[13] C. Cocchi and H. D. Saßnick, Ab initio quantum–mechanical predictions of semiconducting photocathode materials, Micromachines **12**, 22 (2021).
[14] H.-D. Saßnick and C. Cocchi, Electronic structure of cesium-based photocathode materials from density functional theory: performance of PBE, SCAN, and HSE06 functionals, Electronic Structure **3**, 027001 (2021).
[15] J. F. Moulder, W. F. Stickle, P. E. Sobol, and K. D. Bomben, *Handbook of X-ray Photoelectron Spectroscopy* (Perkin-Elmer Corporation, 1992).
[16] L. Soriano and L. Galán, Interaction of Cesium-Potassium Antimonide Photocathode Materials with Oxygen: an X-Ray Photoelectron Spectroscopy Study, Japanese Journal of Applied Physics **32**, 4737 (1993).
[17] I. Martini, E. Chevallay, V. Fedosseev, C. Hessler, H. Neupert, V. Nistor, and M. Taborelli, X-ray photoemission spectroscopy studies of cesium antimonide photocathodes for photoinjector applications, Physics Procedia **77**, 34 (2015).
[18] M. A. H. Schmeißer, S. Mistry, H. Kirschner, S. Schubert, A. Jankowiak, T. Kamps, and J. Kühn, Towards the operation of Cs-K-Sb photocathodes in superconducting RF photoinjectors, Phys. Rev. Accel. Beams **21**, 113401 (2018).
[19] C. D. Wagner, Chemical shifts of Auger lines, and the Auger parameter, Faraday Discuss. Chem. Soc. **60**, 291 (1975).
[20] W. E. Morgan, W. J. Stec, and J. R. Van Wazer, Inner-orbital binding-energy shifts of antimony and bismuth compounds, Inorganic Chemistry **12**, 953 (1973).
[21] J. Jupille, P. Dolle, and M. Besançon, Ionic oxygen species formed in the presence of lithium, potassium and cesium, Surface Science **260**, 271 (1992).
[22] S. J. Yang and C. W. Bates, The role of cesium suboxides in low-work-function surface layers studied by x-ray photoelectron spectroscopy: Ag-O-Cs, Applied Physics Letters **36**, 675 (1980).
[23] C. D. Wagner, D. A. Zatko, and R. H. Raymond, Use of the oxygen KLL Auger lines in identification of surface chemical states by electron spectroscopy for chemical analysis, Analytical Chemistry **52**, 1445 (1980).
[24] N. G. Krishnan, W. N. Delgass, and W. D. Robertson, Electron binding energies of core levels in caesium adsorbed on a nickel (100) surface, Journal of Physics F: Metal Physics **7**, 2623 (1977).
[25] G. Ebbinghaus and A. Simon, Electronics structures of Rb, Cs and some of their metallic oxides studied by photoelectron spectroscopy, Chemical Physics **43**, 117 (1979).
[26] A. Galdi, W. J. I. DeBenedetti, J. Balajka, L. Cultrera, I. V. Bazarov, J. M. Maxson, and M. A. Hines, The effects of oxygen-induced phase segregation on the interfacial electronic structure and quantum efficiency of Cs_3Sb photocathodes, The Journal of Chemical Physics **153**, 144705 (2020).
[27] J. Yeh and I. Lindau, Atomic subshell photoionization cross sections and asymmetry parameters: $1 \leq Z \leq 103$, Atomic Data and Nuclear Data Tables **32**, 1 (1985).
[28] A. Damascelli, Probing the Electronic Structure of Complex Systems by ARPES, Physica Scripta **T109**, 61 (2004), 0307085.